



Article

Ni Catalysts Based on Attapulgite for Hydrogen Production through the Glycerol Steam Reforming Reaction

Nikolaos D. Charisiou ^{1,*}, Victor Sebastian ^{2,3} , Steven J. Hinder ⁴, Mark A. Baker ⁴, Kyriaki Polychronopoulou ^{5,6} and Maria A. Goula ^{1,*} 

¹ Laboratory of Alternative Fuels and Environmental Catalysis (LAFEC),

Department of Chemical Engineering, University of Western Macedonia, GR-50100 Kila, Greece

² Chemical and Environmental Engineering Department, Instituto de Nanociencia de Aragón (INA) and Instituto de Ciencia de Materiales de Aragón (ICMA), Universidad de Zaragoza-CSIC, 50018 Zaragoza, Spain

³ Networking Research Center on Bioengineering, Biomaterials and Nanomedicine, CIBERBBN, 28029 Madrid, Spain

⁴ The Surface Analysis Laboratory, Faculty of Engineering and Physical Sciences, University of Surrey, Guildford GU2 4DL, UK

⁵ Department of Mechanical Engineering, Khalifa University of Science and Technology, Abu Dhabi P.O. Box 127788, UAE

⁶ Center for Catalysis and Separations, Khalifa University of Science and Technology, Abu Dhabi P.O. Box 127788, UAE

* Correspondence: ncharis@teiw.m.gr (N.D.C.); mgoula@teiw.m.gr (M.A.G.); Tel.: +30-24610-68296 (N.D.C. & M.A.G.)

Received: 3 July 2019; Accepted: 25 July 2019; Published: 30 July 2019



Abstract: Attapulgite (ATP, a natural clay) was used as carrier to produce a nickel-based catalyst (Ni/ATP) for the work that is presented herein. Its catalytic performance was comparatively assessed with a standard Ni/Al₂O₃ sample for the glycerol steam reforming (GSR) reaction. It was shown that the ATP support led to lower mean Ni crystallite size, i.e., it increased the dispersion of the active phase, to the easier reduction of NiO and also increased the basicity of the catalytic material. It was also shown that it had a significant effect on the distribution of the gaseous products. Specifically, for the Ni/ATP catalyst, the production of liquid effluents was minimal and subsequently, conversion of glycerol into gaseous products was higher. Importantly, the Ni/ATP favored the conversion into H₂ and CO₂ to the detriment of CO and CH₄. The stability experiments, which were undertaken at a low WGFR, showed that the activity of both catalysts was affected with time as a result of carbon deposition and/or metal particle sintering. An examination of the spent catalysts revealed that the coke deposits consisted of filamentous carbon, a type that is known to encapsulate the active phase with fatal consequences.

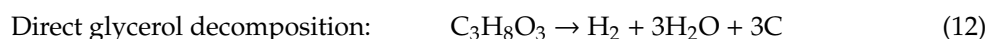
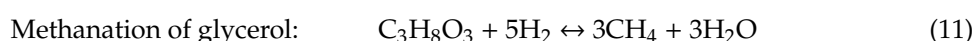
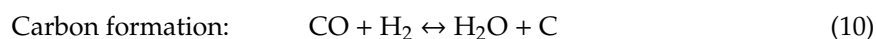
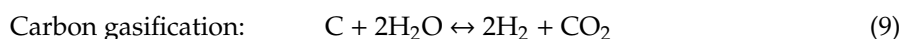
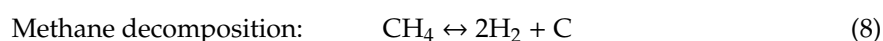
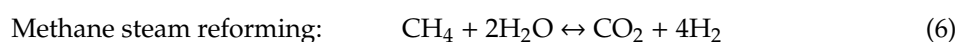
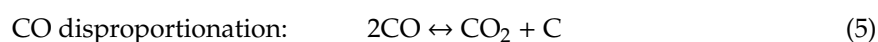
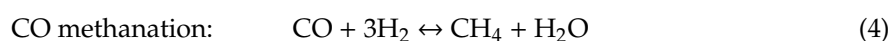
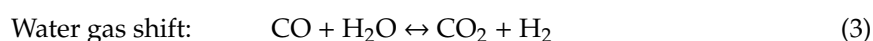
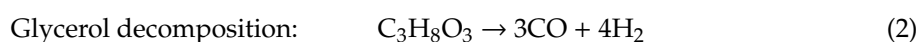
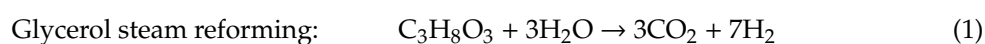
Keywords: attapulgite; natural clays; hydrogen production; Ni catalysts; glycerol; steam reforming

1. Introduction

The need to find an alternative to petro-based sources in the transport sector has provided the impetus for the development of the biodiesel industry, with its production increasing from 774,000 tons in 2000 to 30 million tons in 2016, i.e., in a decade and a half the sector experienced an increase of almost 40-fold [1]. However, the transesterification reaction, which is currently used for the production of the desired esters (biodiesel), also produces significant quantities of glycerol as a by-product (10% of the oil undergoing the reaction) [2]. Despite the fact that pure glycerol is a valuable raw material with over

2000 industrial uses, the glycerol produced from the biodiesel industry contains impurities (such as non-reacted and partially reacted fats, free fatty acids, methanol, esters, and salts), which make its refining and purification highly costly [3]. Thus, crude glycerol is currently treated as an industrial waste, which means that efforts directed towards glycerol's valorization can not only have a significant impact towards helping the biodiesel industry become more competitive, but also further enhance its environmental credentials.

Amongst the different options that have been proposed (Bagheri et al. [4] has provided an excellent review on the topic), the steam reforming of glycerol (GSR) for the production of hydrogen—a clean and renewable energy source—is increasingly drawing the attention of the scientific community (e.g., [5–7]). This is because SR is a mature industrial technology, but also because, as the overall reaction (Equation (1)) shows, every 1 mol of converted $C_3H_8O_3$ can produce 7 mol of H_2 . In comparison, the steam reforming of methane leads to the production of only 4 mol of H_2 per mol of converted CH_4 . The GSR consists of two major steps, i.e., the decomposition of $C_3H_8O_3$ (Equation (2)) and the water-gas shift (WGS) reaction (Equation (3)), however it is also influenced by the occurrence of multiple side reactions (Equations (4)–(12)) and by the formation of different by-products that act as intermediaries during the reaction [8,9]. Moreover, the process also requires a high water to glycerol feed ratio (WGFR), and, as the GSR is a strongly endothermic reaction ($\Delta H^\circ = 123$ kJ/mole), hydrogen production is favoured at elevated reaction temperatures [8,9].



The successful industrial application of the GSR process requires the development of low cost, highly active, and stable catalysts. As noble-based catalysts pose obvious cost related challenges for industrial applications, research efforts have focused on the use of transition metals as the active component. Amongst such metals Ni-based catalysts are the most investigated thus far, because Ni promotes the cleavage of C–C bonds and the WGS reaction (which increases the production of H_2). However, Ni is also known to induce carbon deposition on the catalyst surface during reaction, which affects the system's long term stability [10–14]. Apart from the active phase, the second critical component of any catalyst system is the supporting material, and, as is well understood, its interaction with the active metallic component plays a crucial role in determining catalytic performance. As the GSR takes place at high temperatures, the supporting material that is used should be thermally stable. It should also have a relatively high surface area in order to aid the dispersion of the active phase, and the ability to provide strong metal-support interactions (SMSI) to help maintain the particle size of the active species during reaction. Other important properties include its oxygen storage capacity

(OSC), which can help to minimize carbon deposition during reaction, and surface basicity [15,16]. The efforts to produce stable Ni-based catalysts for the GSR have led to the testing of a variety of different metal oxides, such as Al_2O_3 , ZrO_2 , TiO_2 , SiO_2 , La_2O_3 , and CeO_2 as supporting material, often modified by transition (e.g., ZrO_2 , Y_2O_3), lanthanide (e.g., Ce_2O_3 , La_2O_3 , Sm_2O_3), or alkaline earth metals (e.g., CaO , MgO , BaO) [17–27]. In previously published work by our group [27], we showed that the presence of alkaline earth metals, specifically CaO and MgO , as promoters of $\gamma\text{-Al}_2\text{O}_3$, facilitate the dispersion of the active species, strengthens the interaction between the active phase and the support, and increases the population of basic sites. It also alters the nature of the deposited carbon towards structures that are less graphitic (and thus easier to oxidize), which helps to maintain catalytic stability during long time-on-stream testing.

Among the different materials that may be used as catalyst carriers, clay minerals, such as kaolin, bentonite, sepiolite, montmorillonite, and attapulgite (ATP), are an option worth exploring, as they are non-toxic, have excellent hydrothermal stability, and also high availability (which means that their cost is very low). As such, they have been used as supports in several catalytic applications with encouraging results [28–32]. Jiang et al. [33] tested the performance of Ni/montmorillonite (MMT) catalysts in the GSR between 400–600 °C while using a steam to carbon (S/C) ratio of 3 and concluded that the MMT support favored the dehydrogenation reaction pathway (thus restricting carbon deposition) and inhibited the sintering of the Ni particles. Menor et al. [34] reported on the performance of Ni/sepiolite in the GSR, comparing the activity that was achieved by a catalyst that was prepared by the incipient wetness impregnation method with one that was prepared by a patented precipitation (PP) method. The tests were carried out between 350–700 °C while using a S/C ratio of 3 and the conclusion was that the Ni/PP sample worked better at mild reaction conditions (350–400 °C) due to the higher dispersion of the Ni metallic particles; above 400 °C, the performance of the two samples was very similar.

Attapulgite (ATP, otherwise known as palygorskite) is a hydrated magnesium aluminum silicate clay mineral $[(\text{H}_2\text{O})_4(\text{Mg},\text{Al},\text{Fe})_5(\text{OH})_2\text{Si}_8\text{O}_{20}\cdot 4\text{H}_2\text{O}]$ with reactive hydroxy groups on its surface [35], which consists of tetrahedral (Si^{4+}) and octahedral (Al^{3+}) sheets. The tetrahedral sheets are inverted in the apical direction in adjacent ribbons, alternating with rectangular channels along the fiber axis, while the octahedral sheets (that can be either dioctahedral or trioctahedral) are discontinuous at each inversion of the tetrahedron [31]. Chen et al. [35] investigated the performance of different transition metal (Ni, Cu, Co, or Fe) catalysts that are based on ATP in the GSR in the temperature range 400–750 °C while using a Water Glycerol Feed Ratio (WGFR) of 3 (molar) and a Weight Hour Space Velocity (WHSV) of 6.46 h^{-1} and reported that H_2 selectivity followed the order $\text{Ni}/\text{ATP} > \text{Co}/\text{ATP} > \text{Cu}/\text{ATP} > \text{Fe}/\text{ATP}$; they attributed these results to the superior capacity of Ni and Co to rupture the C-C bond and facilitate the WGS reaction. The same group [36] also reported on the performance of monometallic Ni and bimetallic Ni-Co, Ni-Cu, and Ni-Zn catalysts supported on ATP while using a WGFR of 9, and a Gas Hour Space Velocity (GHSV) of 9619 h^{-1} . The authors conducted short (3 h, at 500, 600, and 700 °C) and long (30 h, at 600 °C) time-on-stream experiments and found that glycerol conversions and H_2 yield were higher for the bimetallic catalysts in comparison with the Ni/ATP. For example, during the short time-on-stream experiments at 600 °C, glycerol conversion to gaseous products followed the order $\text{Ni-Cu}/\text{ATP}$ (73.4%) > $\text{Ni-Co}/\text{ATP}$ (70.4%) > $\text{Ni-Zn}/\text{ATP}$ (67.6%) > Ni/ATP (66.8%). However, they also reported that the Ni-Zn/ATP catalyst was more stable than the other samples during the long time-on-stream experiments (that they attributed to improved metal-support interaction), while the monometallic Ni/ATP deactivated rather quickly. The authors did not provide an analysis of the liquid products that were obtained during the reaction in the works that are mentioned above [35,36].

Based on this background, the present investigation reports on the catalytic activity and time-on-stream stability during the GSR of a Ni/ATP catalyst and compares it to that of a Ni catalyst that was supported on commercially available $\gamma\text{-Al}_2\text{O}_3$. Both of the catalysts were prepared by the wet impregnation technique and had a nominal Ni loading of 8 wt%. The characterization techniques that

were used for the identification of the catalysts' surface and bulk properties, included N₂-physisorption, Inductively Coupled Plasma Atomic Emission Spectroscopy (ICP–AES), X-Ray Diffraction (XRD), H₂ Temperature Programmed Reduction (H₂–TPR), CO₂ and NH₃ Temperature Programmed Desorption (CO₂–TPD, NH₃–TPD), X-Ray Photoelectron Spectroscopy (XPS), Transmission Electron Microscopy (TEM), and High-Angle Annular Dark-Field Scanning Transmission Electron Microscopy (STEM-HAADF). The catalytic experiments were conducted between 400 and 750 °C while using a WGFR of 20/1, and aimed at identifying the effect of temperature on the total conversion of glycerol, the conversion of glycerol to gaseous products, and also on the selectivity towards gaseous and liquid products. This necessitated the quantification not only of the gaseous products produced during the reaction, but also of the main liquid effluents. The time-on-stream experiments were conducted for 20 h under harsh reaction conditions (WGFR = 9), in order to induce carbon deposition and catalyst deactivation.

2. Results

2.1. Materials Characterization

2.1.1. Chemical Analysis and Textural Properties

Table 1 presents information regarding the Specific Surface Area (SSA) and pore volume (V_p) of the untreated and calcined catalyst carriers. Both of the supports exhibit high SSA's (281 and 220 m² g^{−1} for the Ni/Al and Ni/ATP, respectively), which quite substantially drop following the calcination procedure (195 and 173 m² g^{−1} for the Ni/Al and Ni/ATP, respectively). Elemental analysis of the calcined ATP support revealed the presence of SiO₂, Al₂O₃, Fe₂O₃, MgO, MnO, TiO₂, CaO, Na₂O, and K₂O (51.9, 5.2, 11.0, 13.0, 0.2, 0.3, 3.8, <0.05, 0.3%, respectively; LOI = 14.0%).

Table 1. Specific Surface Area (SSA), Por Volume (V_p) of the supports used herein and elemental analysis of attapulgite (ATP).

Support	SSA (m ² g ^{−1})	V _p (mL g ^{−1})
Al (untreated)	281	0.65
Al (calcined)	195	0.65
ATP (untreated)	220	0.70
ATP (calcined)	173	0.57

Figure 1 presents the pore size distribution and the N₂ adsorption–desorption isotherms of the ATP and alumina Ni supported catalysts. The Ni/Al and Ni/ATP isotherms are of type IV and type III, respectively, according to the IUPAC classification. The particular type of Ni/Al isotherm is associated with mesoporous materials (type IV), whereas the one of the Ni/ATP isotherm is the regular type of isotherm for clays [37]. The hysteresis loop for the Ni/ATP catalyst is H3 type and it can be associated with the presence of aggregated platelike particles, forming slit pores [38]. In the case of Ni/Al, the hysteresis loop is type H2, indicating rather disordered mesopores.

Table 2 shows the textural properties (specific surface area, pore volume, and pore diameter) of the catalysts. The specific surface area (SSA, m²/g) for the Ni/Al and Ni/ATP catalysts were found to be 158 (136) and 140 (17.5) m²/g, following calcination (reduction), respectively. In the literature, there are reports on the SSA of ATP that reach the value of 140 m²/g [39], which is in good agreement with the value over the calcined Ni/ATP catalyst of this study. Though, the textural characteristics of natural materials do heavily depend on their origin (usually dictates composition) and sample history (chemical pretreatment, thermal pretreatment, doping type, and doping extent). In their interesting study of attapulgite evolution under different thermal treatments, Boudriche et al. [40] reported a dramatic drop in the surface area from 125 m²/g (raw ATP) to 28.6 m²/g (following heat treatment at 800 °C) to 1.6 m²/g (following heat treatment at 1000 °C). In our study, the ATP support was pretreated/calcined at 800 °C for 4 h before the Ni (7 wt%) impregnation process took place. The latter process can be

another reason for porosity blocking in the ATP porosity structure. Sidheswaran et al. [41], in their study of an Indian ATP, attributed the SSA drop to the formation of two crystalline phases, forsterite (MgSiO_4) and enstatite (MgSiO_3). In another study by Frini-Srasra et al. [42], where a Tunisian ATP was examined, it was reported a small SSA increase with the temperature followed by a decrease when the temperature was further increased. The initial increase was linked to the removal of water, whereas a coalescence of particles happening at the higher temperatures led to the final SSA drop. The pore size distribution for both of the catalysts of this study is attributed to the profound mesoporous nature for both of the materials with a 10–50 and 10–70 nm size for Ni/Al and Ni/ATP, respectively. The pore volume was found to be 0.58 (0.32) and 0.51 (0.09) cm^3/g for the Ni/Al and Ni/ATP following calcination (reduction), corroborating a rather high pore volume for both catalysts following calcination that is transformed to a moderate high and a rather low pore volume, for the Ni/Al and Ni/ATP, respectively, following reduction. It is noted that both calcined catalysts had almost identical metal loadings, which were measured at 7.14 wt.% for the Ni/Al and 7.10 wt.% for the Ni/ATP.

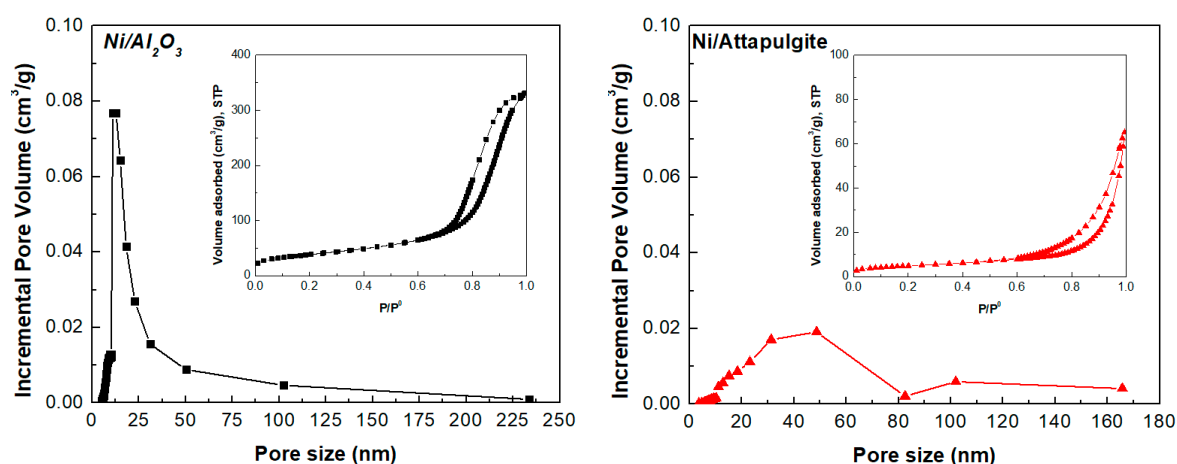


Figure 1. Pore size distribution and N_2 adsorption-desorption isotherms (inset) of Ni/Al and Ni/ATP catalysts.

Table 2. Physicochemical, structural, and textural properties of calcined and reduced catalysts.

Catalyst	Calcined Catalysts				Reduced Catalysts			
	Metal Loading (Ni, wt.%) ¹	SSA (m^2g^{-1}) ²	Pore Volume (cm^3/g) ²	SSA (m^2g^{-1}) ²	Pore Volume (cm^3/g) ²	Av. Pore Width (nm) ²	Ni^0 Mean Crystallite Size (nm) ³	Ni^0 Dispersion (%) ⁴
Ni/Al	7.14	158	0.58	136	0.32	20.1	14.4	4.6
Ni/ATP	7.10	140	0.51	17.5	0.09	17.5	6.2	10.7

Calculated using: ¹ ICP, ² N_2 adsorption-desorption, ³ TEM, ⁴ the Vannice method.

Figure 2 presents the XRD diffractograms that were obtained over the Ni/Al (Figure 2a) and Ni/ATP (Figure 2b) catalysts following calcination and reduction (both undertaken at 800 °C). In the case of Ni/Al catalyst, there is no significant difference in the XRD patterns following calcination or reduction. It is noteworthy that the majority of the catalyst exists in the NiAl_2O_4 spinel type phase and only traces of Ni^0 (metallic phase, peaks at 44.5° and 51.8° (JCPDS PDF# 04-0850)) appeared after reduction of the catalyst. In the case of Ni/ATP catalyst, the presence of NiO (peaks at 37.2° and 43.3° (JCPDS PDF# 44-1159)) in the calcined catalyst is profound and its subsequent reduction leads to the clear presence of Ni^0 (metallic phase, peaks given above). This finding is important from the catalysis point of view, as trapping Ni inside the support through the formation of a Ni-containing mixed oxide (spinel phase) leads to an apparent loss of active metal for the reaction of interest, as it will be discussed later. It can be found that the peaks at $2\theta = 20.5^\circ, 24.3^\circ, 25.5^\circ, 27.7^\circ, 29.8^\circ, 33.2^\circ, 35.7^\circ, 42.9^\circ, 56.8^\circ,$ and 62.9° in ATP are in good agreement with palygorskite/attapulgite (JCPDS PDF#

31-0783) phase, and the peaks at $2\theta = 30.6^\circ$, 45.4° , 50.9° , and 52.3° may belong to dolomite (JCPDS PDF# 99-0046). It is noted that the ICP elemental analysis of the calcined ATP carrier revealed the presence of both CaO and MgO, which can explain the dolomite structure detected herein. The peaks at $2\theta = 20.8^\circ$ and 26.6° correspond to SiO₂ quartz phase. The fact that the peaks of the calcined Ni/ATP are maintained following the reduction is important, as it shows the preservation of ATP structure. Moreover, the presence of CaO and MgO in ATP is expected to have a beneficial effect on the dispersion of the active phase and increase the population of the basic sites [27].

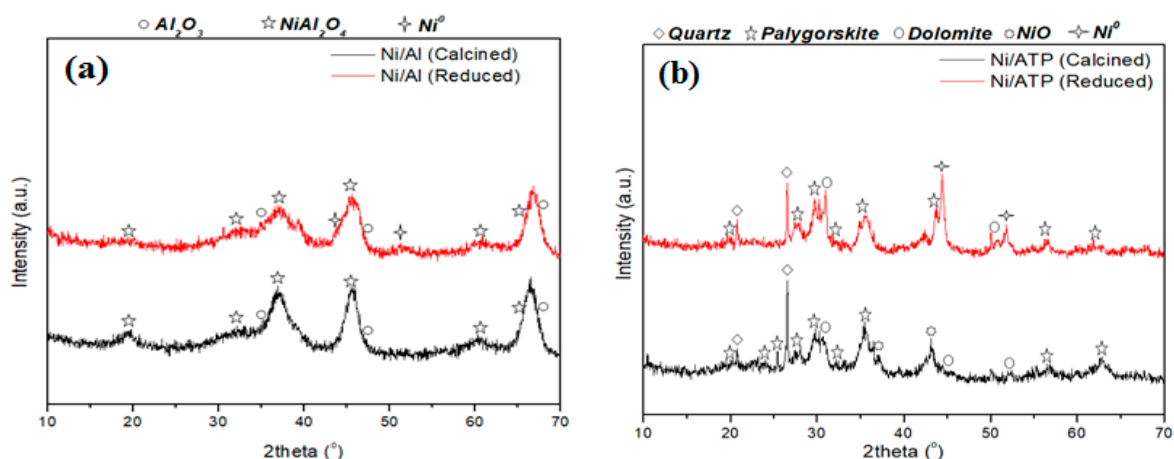


Figure 2. X-Ray Diffraction (XRD) patterns of the calcined and reduced (a) Ni/Al and (b) Ni/ATP catalysts.

2.1.2. Acid and Basic Properties

Figure 3a presents the CO₂-TPD profiles that were obtained over the Ni/Al and Ni/ATP catalysts. As ATP is a 2:1 magnesium aluminosilicate (phyllosilicate), it is expected to present rich basic properties/sites. Based on the results in Figure 3a, the basic sites can be classified into three categories that are based on the desorption peak region. In particular, the one at low temperature zone (up to 200 °C), the one at the 200–450 °C temperature, and the one at high temperature (>500 °C) could be attributed to CO₂ desorption from the weak, medium, and strong basic sites, respectively. By a one-to-one comparison of the two catalysts of interest, it can be stated that Ni/Al presents mostly low and medium strength basic sites, with a minor contribution from strong ones. On the other hand, ATP presents a higher population of medium and strong basic sites. The profiles received in this study are in good agreement with the ones that were reported by Wu et al. [43].

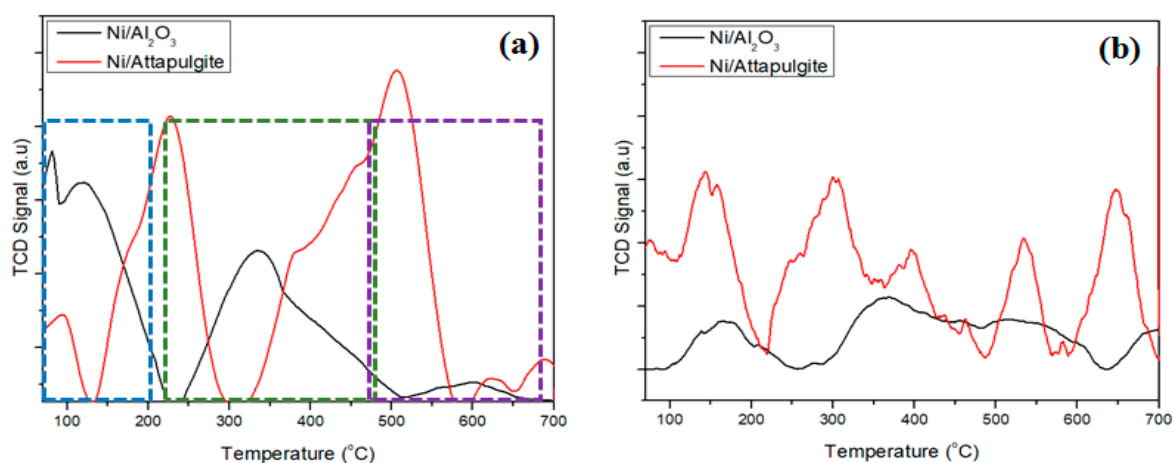


Figure 3. (a) CO₂-TPD and (b) NH₃-TPD profiles of the Ni/Al and Ni/ATP catalysts.

Figure 3b presents the NH₃-TPD profiles of the Ni/Al and Ni/ATP catalysts. Ni/ATP presents a wide distribution of weak, medium, and strong acid sites, as indicated by the peaks at 150, 300, 400, and >500 °C. Similarly, Ni/Al catalyst exhibits a polydispersity of acid sites strength, with a much lower population though. In agreement with Huang et al. [39], the weak acid sites are of Brønsted type, whereas the medium and strong ones are of Lewis type.

2.1.3. Ni Species Reducibility

The reducibility of Ni/Al and Ni/ATP catalysts was studied while using H₂-TPR. Figure 4 presents the H₂-TPR profiles for both of the catalysts. There are three well defined peaks for each one of the catalysts. In particular, for the Ni/Al catalyst, the peaks maxima are at the 220 °C, 450 °C, and 700 °C, corresponding to the well dispersed NiO particles loosely interacting with alumina support (free NiO particles), NiO particles in close interaction with the support and spinel type phase (nickel aluminate), respectively. These reduction profiles are in full agreement with Rosha et al. [44]. In the case of Ni/ATP, the peak at 220 °C (previously discussed) is almost vanishing, whereas the other two peaks are profoundly shifted to lower temperatures, namely at 370 °C and 575 °C, implying for either smaller NiO particles (better dispersion of Ni on ATP when compared to Al₂O₃ support) or lower interaction of NiO with the underlying support leading to a much easier reduction of NiO. The peak at 370 °C can be attributed to ‘free’ NiO particles, which is in agreement with Wang et al. [29]. The easier reduction of NiO when ATP is used as carrier is supported by the XRD results, where NiO phase can be found only in the case of Ni/ATP catalyst, whereas in the case of Ni/Al catalyst the strong interaction between Ni and support leads to the formation of spinel type of mixed oxides (NiAl₂O₄).

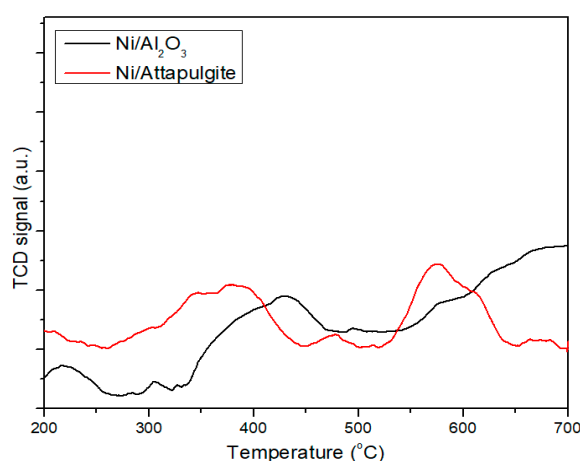


Figure 4. Temperature Programmed Reduction (TPR) profiles of the Ni/Al and Ni/ATP catalysts.

2.1.4. Surface Analysis

Table 3 provides the quantified elemental compositions and peak positions from XPS analysis of the Ni/Al and Ni/ATP catalyst. The XPS Ni 2p spectra for Ni/ATP and Ni/Al and O 1s spectrum for Ni/ATP are given in Figure 5. The wide scan spectrum of the Ni/ATP catalyst is included as a Supplementary file (Figure S1).

Table 3. X-Ray Photoelectron Spectroscopy (XPS) determined surface elemental concentrations and core level peak maxima for the Ni/ATP and Ni/Al catalysts.

Catalyst	Element	O (1s)	Si (2p)	Al (2p)	Mg (1s)	Ca (2p)	Ni (2p)	C (1s)
Ni/ATP	Elemental conc. (at.%)	57.3	17.7		4.4	5.8	6.4	8.4
Ni/ATP	Binding energy (eV)	531.9	102.5		1304.3	347.4	855.9	285.0
Ni/Al	Elemental conc. (at.%)	68.5		27.3			2.8	1.4
Ni/Al	Binding energy (eV)	531.0		74.1			856.0	285.0

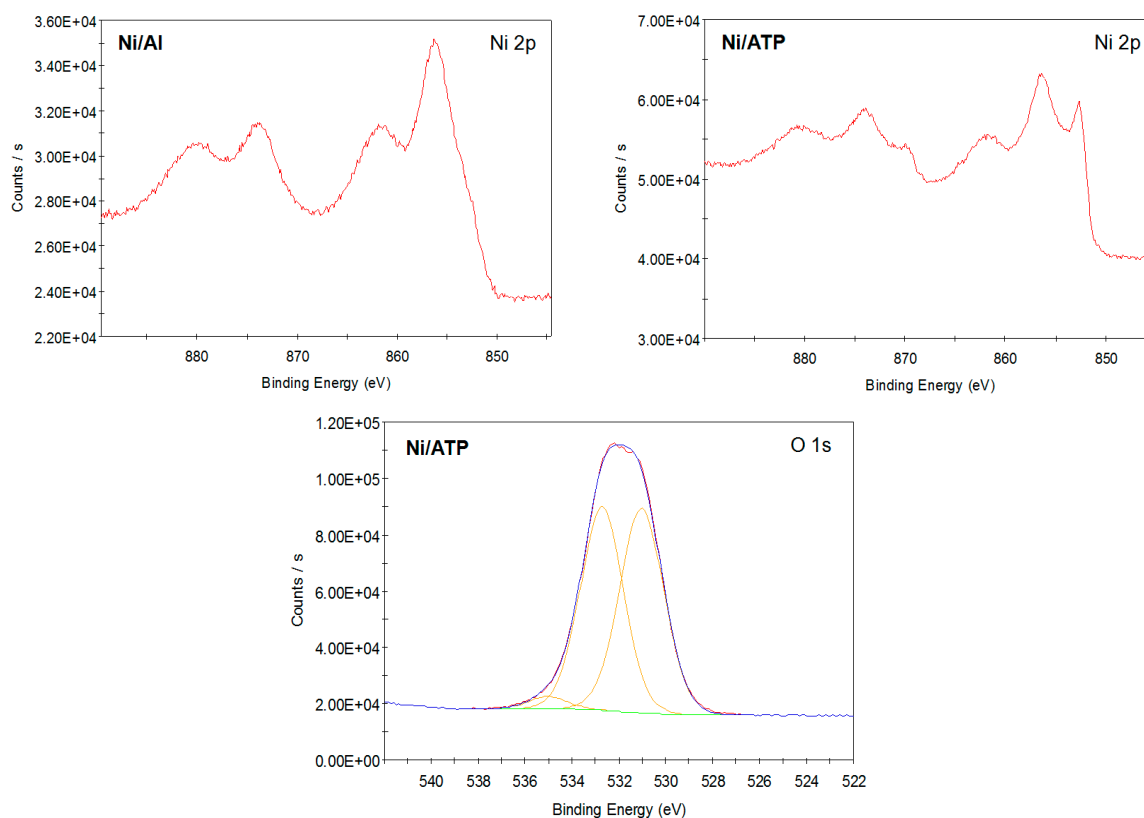


Figure 5. XPS Ni 2p for the reduced Ni/Al and Ni/ATP catalysts and O 1s for the reduced Ni/ATP.

The ATP composition varies from that expected $[(\text{H}_2\text{O})_4(\text{Mg}, \text{Al}, \text{Fe})_5(\text{OH})_2\text{Si}_8\text{O}_{20} \cdot 4\text{H}_2\text{O}]$, in that neither Al or Fe are observed in the XPS spectra and Ca is present instead. The composition of clay minerals is known to vary, according to the particular source and location of origin and the presence of Ca and other exchangeable ions in ATP are shown in the Data Handbook for Clay Minerals and Other Non-Metallic Materials [45]. Therefore, it would appear that Al and Fe are being replaced by Ca within the ATP mineral used in this work. From the nominal molecular formula, the Si:(Mg, Al, Fe) concentration ratio should be 8:5. Thus, if Ca is replacing Al/Fe within the ATP structure, then the Si:(Mg, Ca) ratio should be 8:5 (or 1.6), whereas the XPS determined Si:(Mg, Ca) ratio is 8:4.6 (or 1.74). The nominal and experimentally determined ratios are very similar, which suggests that Ca is indeed substituting for Al and Fe within the ATP structure. With regard to the binding energies of the cations, the Si $2p_{3/2}$ and Mg 1s peaks occur at binding energies of 102.5, and 1304.3 eV, respectively. There have been very few XPS studies of ATP in the literature, but these binding energies compare well to the values of 103.0 and 1304.0, respectively, given for ATP (palygorskite) by Kloprogge and Wood [46]. These authors have also noted that the Ca 2p peak occurs at around 347.2 eV when Ca is exchanged for one of the cations in various clay minerals, which is very similar to the 347.4 eV value that was observed for the ATP in this work. Barr et al. [47] have noted for aluminosilicate minerals that as the Al/Si concentration ratio in the mineral increases, the binding energy of the Si 2p peak decreases, due to the more ionic Al-O bond giving rise to the Si-O bond becoming more covalent in character compared to pure silica or silicate units. Similarly, exchanging Ca (electronegativity = 1.00) for Al (electronegativity 1.61) in the ATP structure may explain why the Si 2p binding energy is 0.5 eV lower than that observed for ATP by Kloprogge and Wood [46]. The O 1s peak for ATP in Figure 5 is different from that given for ATP by Kloprogge and Wood [46]. In the ATP that was employed here, the O 1s peak can be peak fitted into two strong components at 530.8 eV and 531.9 eV. This compares to a smaller component at 531.4 eV and a larger component at 532.6 eV in the ATP that was examined by Kloprogge and Wood [46]. They attributed the larger intensity peak at 532.6 eV to Si atoms within the ribbon structure, and the smaller intensity peak at 531.4 eV to oxygen atoms connecting the ribbons.

These authors also show the presence of smaller peaks at higher binding energies that are associated with OH^- and H_2O , as would be expected. The difference in the O 1s spectra for the ATP examined here is most probably associated with the presence of oxide/hydroxide species on the nickel surface and/or the substitution of Ca for Fe and Al in this clay.

The Ni 2p peak for Ni/ATP shows the clear presence of the lower binding energy metallic Ni peak at 853 eV and a peak maximum at 855.9 eV, which can be attributed to nickel silicate/ Ni_2O_3 [48]. Nickel is present at 6.5 at.%. In comparison, the Ni 2p peak for Ni/Al shows a much weaker presence of metallic nickel. The presence of the main Ni $2p_{3/2}$ peak at a binding energy of 856.0 eV is associated with the presence $\text{NiAl}_2\text{O}_4/\text{Ni}_2\text{O}_3$ [19], and the metallic Ni only results in a shoulder being present at around 853 eV. Nickel is present at 2.8 at.%.

Figure 6 presents the STEM-HAADF images (Figure 6a), EDS analysis (Figure 6b), and particle size distribution histogram (Figure 6c) for the reduced Ni/Al catalyst. Figure 7 depicts the same information for the reduced Ni/ATP catalyst. For both catalysts, the Ni nanoparticles are of pseudo-spherical shape and rather homogeneously distributed on the catalytic surface. Importantly, the mean particle size was found to be substantially lower on the Ni/ATP catalyst (6.2 ± 2.6 nm), in comparison to the Ni/Al (14.4 ± 4.5 nm).

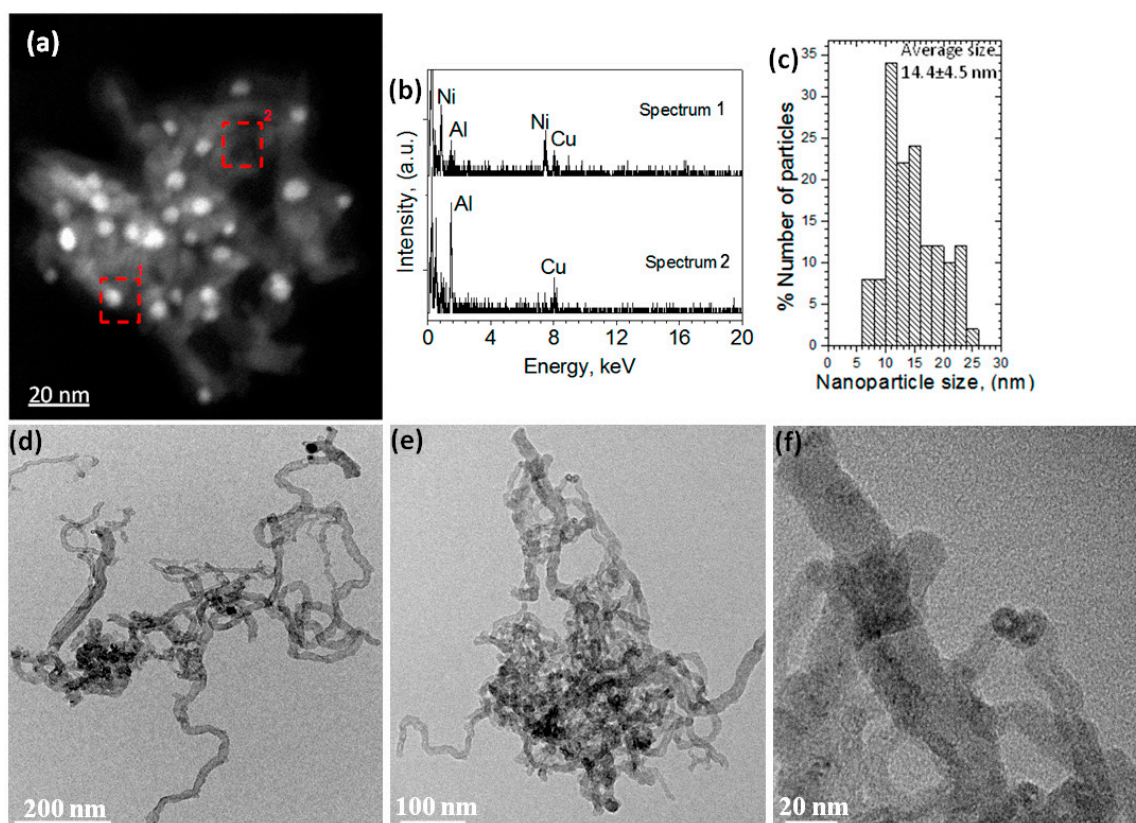


Figure 6. Ni/Al catalyst: (a) High-Angle Annular Dark-Field Scanning Transmission Electron Microscopy (STEM-HAADF) images with Z-contrast (heavy atoms have high brightness), (b) energy dispersive X-ray spectroscopy (EDS) spectra of area marked in (a), (c) Particle size distribution histogram, (d–f) TEM images of carbon nanostructures.

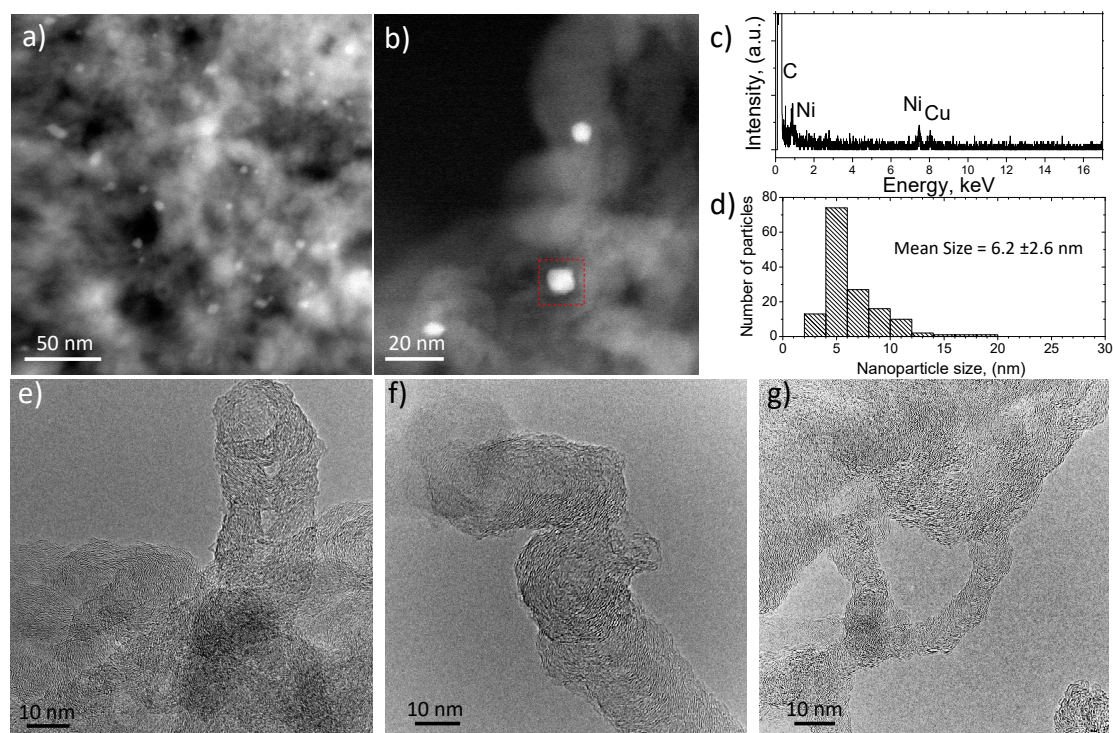


Figure 7. Ni/ATP catalyst: (a,b) STEM-HAADF images with Z-contrast (heavy atoms have high brightness), (c) EDS spectrum of area marked in (b), (d) Particle size distribution histogram, and (e–g) HRTEM images of carbon nanostructures.

2.2. Catalytic Performance

Figure 8a shows the influence of reaction temperature on the total conversion of glycerol ($X_{C_3H_8O_3}$, %) and the conversion of glycerol into gaseous products ($X_{C_3H_8O_3 \text{ gaseous}}$, %) for the catalysts and the supports that were tested under experimental protocol #1. In terms of $X_{C_3H_8O_3}$, the Ni/ATP achieves a 91% conversion at 400 °C, which rises to 94% at 750 °C. For the Ni/Al, this value is lower at 400 °C (85%), but, as the temperature increases to 750 °C, it also reaches 94%. The supports also show high $X_{C_3H_8O_3}$ values with ATP converting 82% of glycerol at 400 °C (rising to 91% at 750 °C) and alumina converting 70% of glycerol at the same temperature (rising to 84% at 750 °C). The high glycerol total conversion that was observed for all samples is due to the simultaneous occurrence of the GSR with the thermal decomposition of glycerol. The latter involves thermal cracking reactions before contact between glycerol and the catalytic material and also acid-base catalyzed reactions that take place at the acidic and basic sites of the supporting material [49,50].

The endothermic nature of the reaction can be clearly seen when observing the conversion of glycerol into gaseous products (Figure 8a). Notably, the Ni/ATP catalyst produces more gaseous products than the Ni/Al up to 700 °C; after this temperature, their performance is similar. The same observation can be made in regards to the bare supports, i.e., that ATP produces higher amounts of gaseous products than bare alumina. These results can be understood on the basis of the higher metal dispersion that was observed for the Ni/ATP catalyst (Electron microscopy and XPS measurements), which favours the conversion of glycerol into gaseous products. In turn, the higher metal dispersion can be related to the presence of MgO and CaO in the ATP support, with previously published works [27,51,52], arguing that the use of alkaline earth metals as promoters has a beneficial effect to this important catalytic property.

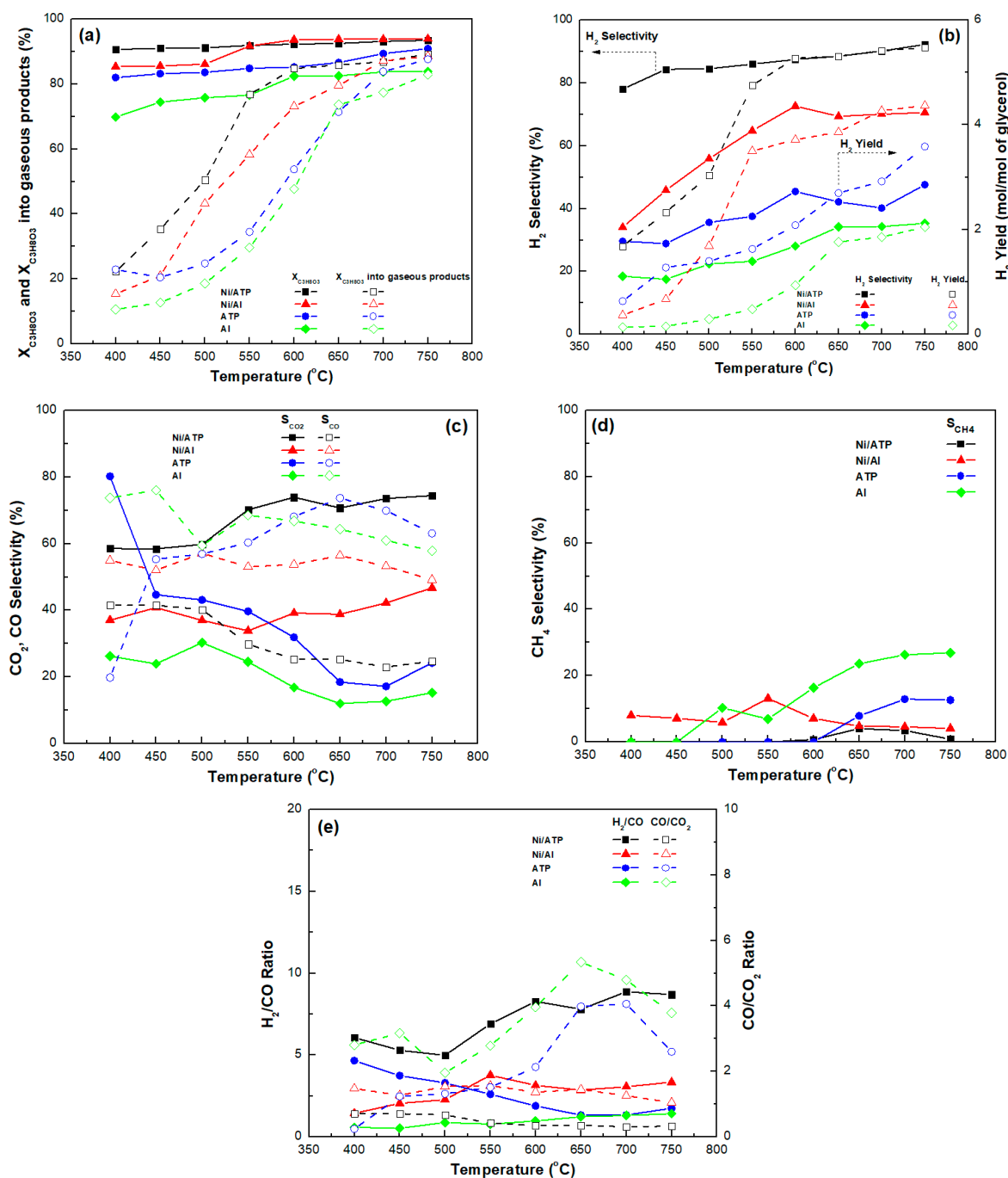


Figure 8. (a) Total glycerol conversion and glycerol conversion into gaseous products, (b) H₂ selectivity and yield, (c) CO₂ and CO selectivity, (d) CH₄ selectivity, and (e) H₂/CO and CO/CO₂ molar ratios, for the catalysts and supporting materials tested herein (samples tested under experimental protocol #1).

Figure 8b shows the effect of reaction temperature on hydrogen selectivity and yield for both catalytic materials and supports. It is obvious that H₂ production is significantly higher for the Ni/ATP sample in comparison to the Ni/Al. In fact, the former catalyst attains a very high S_{H_2} value at low temperatures (78% at 400 °C), which steadily rises as the temperature increases (reaching 92% at 750 °C). In contrast, not only is the S_{H_2} value for the Ni/Al catalyst considerably smaller at low temperatures (34% at 400 °C), but it also reaches a plateau of approximately 75% around 600 °C. Similarly, the hydrogen yield that was obtained for the Ni/ATP catalyst (1.7 mol at 400 °C, increasing to 5.5 mol at 750 °C) is considerably higher in comparison to the Ni/Al (0.4 mol at 400 °C,

increasing to 4.4 mol at 750 °C) for the entire temperature range under investigation. It is worth noting that the maximum value that Y_{H_2} can take, as predicted by thermodynamics, is 6.2 mol [53]. Similarly, the ATP support shows higher S_{H_2} and Y_{H_2} values in comparison with the bare alumina. The improved performance of the Ni/ATP can be understood on the basis of its observed increased basicity (TPD results), which favours the steam to carbon reaction (thus increasing carbon gasification) and helps to suppress cracking and polymerization reactions [54,55].

Figure 8c depicts the influence of reaction temperature on the CO_2 and CO selectivity for both catalytic and supporting materials tested herein. It is obvious that only the Ni/ATP sample is more selective towards CO_2 , and that the Ni/Al and the supports are more selective towards CO. This finding suggests that the enhanced basicity of the Ni/ATP provides a catalyst with improved ability to transform OHCs into H_2 and CO_2 . Figure 8d shows CH_4 selectivity in relation to temperature for all of the materials investigated. For the Ni/ATP, CH_4 selectivity takes practically the value of zero for the entire temperature range under investigation. The same is true for the ATP support up to 600 °C, above which S_{CH_4} gradually increases, reaching a value of 13% at 750 °C. S_{CH_4} is also quite low for the Ni/Al catalyst (ranges between 4–13%), but it rises with temperature for the bare alumina support, reaching a value of 27% at 750 °C. These findings can be attributed to the high WGFR that was used during experimental protocol #1, as the excess steam facilitates the methane steam reforming reaction [56]. Moreover, the Ni based catalysts seem to have the capacity to reform the CH_4 that was produced during the decomposition of glycerol into hydrogen and carbon monoxide. Methane decomposition is also likely at higher temperatures, producing H_2 , but also carbon.

Figure 8e shows the relationship between temperature and the H_2/CO and CO/CO_2 molar ratios in the gaseous products' mixture. For the Ni/ATP catalyst, there is a gradual increase of the H_2/CO molar ratio, with temperature from approximately 6 (at 400 °C) to about 9 (at 750 °C). For the Ni/Al catalyst an almost steady value, between 2 and 3, can be witnessed irrespective of reaction temperature. As for the CO/CO_2 molar ratio, it is close to zero for the Ni/ATP and it is quite stable for the Ni/Al catalyst (again 2–3). In regards to the supports, they both show negligible H_2/CO values, but the CO/CO_2 values increase with temperature up to about 650 °C, above which temperature this ratio seems to be declining.

Figure 9 presents the selectivity towards the main liquid products for the catalytic samples and the supports tested while using experimental protocol #1. It should be noted that, only the main liquid effluents produced during reaction, i.e., acetaldehyde, acrolein, acetone, allyl alcohol, acetic acid, and acetol have been quantified. The effluents detected in trace amounts included 2-Cyclopenten-1-one; propylene glycol; Phenol; 2-Cyclopenten-1-one, 2-methyl; Propanoic Acid; 2,3-Butanedione; 1,2-Ethanediol; 2-Cyclohexen-1-one; 1,3-Dioxan-5-ol; and, Phenol,2-methyl. As mentioned previously, some of the products detected may also act as intermediaries, which further complicates the GSR process. In any case, it is obvious from Figure 9 that no liquid effluents are produced by the Ni/ATP catalyst over 550 °C. In contrast, the Ni/Al catalyst is quite selective towards acetone, allyl alcohol, and acetaldehyde as high as 650 °C; beyond this temperature the production of liquids effluents is also eliminated. Regarding the supports, ATP stops producing effluents at 700 °C; at that temperature, the main liquid products are acetol, acetone, and allyl alcohol. The alumina supports produces liquid effluents for the entire temperature range under investigation, with the main products above 700 °C being acetol, acetone and acetic acid.

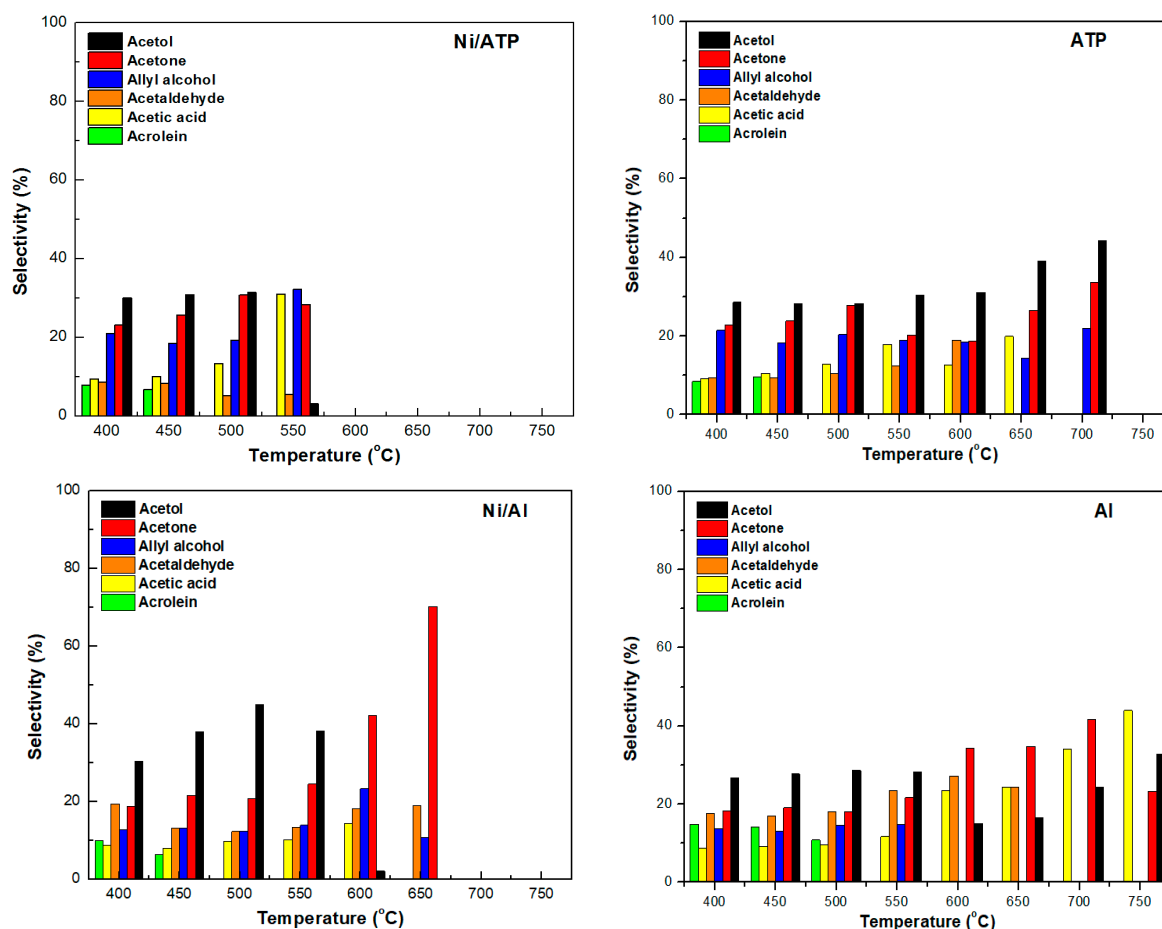


Figure 9. Liquid product selectivity for all samples tested herein (samples tested under experimental protocol #1).

The results that are presented herein show that the reaction pathway followed by the Ni/ATP catalyst leads to fast C-C breaking, which is followed by the formation of CO, and then the occurrence of the WGS reaction. The latter reaction leads in turn to the production of higher amounts of H₂ and CO₂. This conclusion is supported by previously published works, which reported that the use of basic materials (such as ATP), as catalytic supports enhances the production of gaseous products (consequently H₂). In contrast, the use of acidic materials (such as alumina) favors the dehydration and dehydrogenation reactions, which lead to the production of oxygenates (such as acetol, acrolein, acetaldehyde, and acetic acid) [27,55,57]. Given that the molecule of glycerol is thermally unstable, the GSR is also influenced by pyrolysis phenomena, which means that the intermediates that were formed by glycerol cracking are reformed on the catalysts' surface [50].

2.3. Catalytic Stability

Figure 10 presents the results that were obtained during the time-on-stream-experiments (experimental protocol #2). Although the WHSV was kept at 50,000 mL g⁻¹ h⁻¹, i.e., the same with experimental protocol #1, the WGFR was reduced to 9. This made the experimental conditions more severe, as the aim was to induce catalyst deactivation and carbon deposition. Figure 10a shows the progress of the total conversion of glycerol and the conversion of glycerol into gaseous products with time. For the Ni/ATP catalyst X_{C₃H₈O₃} remains relatively stable for approximately 7 h; it then begins to quite sharply drop. For the Ni/Al catalyst, the drop in X_{C₃H₈O₃} is immediate, but after approximately 7 h, it starts diminishing at a much slower pace. For both catalysts, the X_{C₃H₈O₃} gaseous also monotonically drops for the duration of the stability tests. This behaviour indicates that both

catalysts are losing the capacity to promote the C-C rupture, which in turn is evidence that some of the active metallic phase (Ni) is lost to the reactants, due to the deposition of carbon. An examination of the spent catalysts using TEM showed that only the Ni/Al experienced extensive sintering of the active phase, as the Ni mean particle size increased from 14.4 ± 4.5 nm to 43.1 ± 50.1 nm. In contrast, the mean Ni particle size remained virtually unchanged for the Ni/ATP (it was measured at 6.2 ± 2.6 nm on the reduced catalyst and 5.3 ± 2.4 nm on the spent sample).

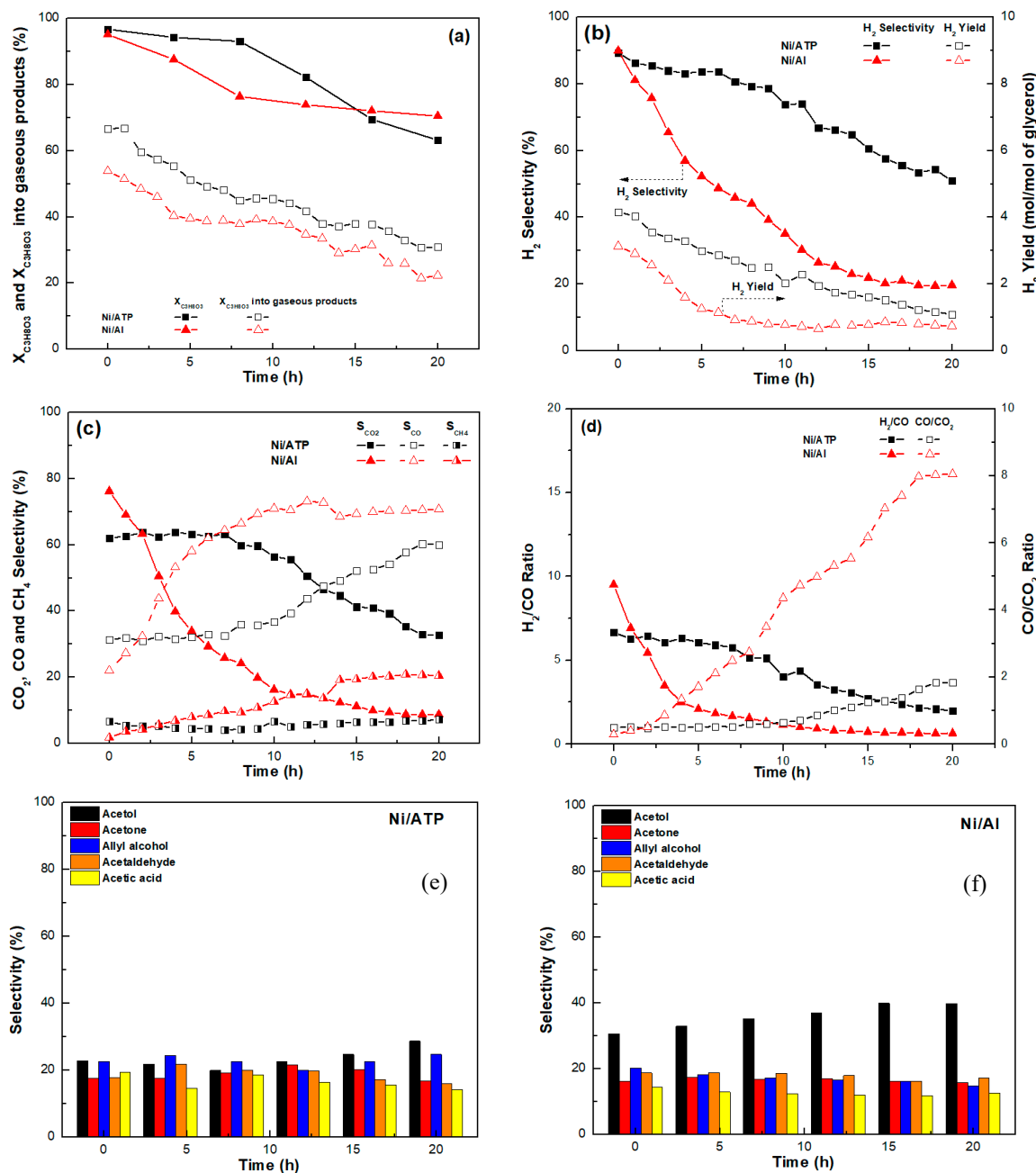


Figure 10. Time on stream experiments for the Ni/Al and Ni/ATP catalysts: (a) Total glycerol conversion and glycerol conversion into gaseous products, (b) H_2 selectivity and yield, (c) CO_2 , CO and CH_4 selectivity, (d) H_2/CO and CO/CO_2 molar ratios, and (bottom) Liquid effluents (samples (e,f) tested under experimental protocol #2).

Figure 10b depicts the effect of time-on-stream on hydrogen selectivity and yield. Both values (i.e., selectivity and yield) drop quite sharply although the Ni/ATP catalyst produces more hydrogen than the Ni/Al, which points to a weakening of the WGS reaction with time. Moreover, for both catalysts, selectivity towards CO₂ decreases (and consequently S_{CO} increases), but for the Ni/Al this occurs almost immediately, while it occurs after approximately 7 h for the Ni/ATP and it is less drastic (Figure 10c). This has an effect on the H₂/CO and CO/CO₂ molar ratios in the gaseous products' mixture (Figure 10d) with the H₂/CO for the Ni/Al dropping sharply, while the CO/CO₂ dramatically increases. The Ni/ATP follows the same trend (i.e., decrease in the H₂/CO and increase CO/CO₂), but at a much-reduced rate. In addition, while S_{CH₄} remains relatively stable for the Ni/ATP, it increases with time for the Ni/Al. Notably, at this increased WGFR, both catalysts produce a significant amount of liquid effluents.

The results presented above indicate that the use of lower WGFR led to significant carbon deposition, and subsequently to catalyst deactivation. For the Ni/ATP, this occurred, despite using a support with enhanced basicity characteristics that helped to achieve a small mean Ni particle size. Chen et al. also observed the quite rapid deactivation of the Ni/ATP catalyst [36]. The examination of carbon deposits for the spent catalysts reported herein, while using TEM and HR-TEM, revealed the heavy formation of filamentous coke on both samples (Figure 6d–f for the Ni/Al and Figure 7e–g for the Ni/ATP). These filaments appear as Multi Wall Carbon Nano Tubes (MWCNT), hollow in the centre, with several graphene layers. As is well understood, this type of carbon encapsulates the Ni particles and it is hard to oxidize during reaction. This means that the active particles are no longer available to the reactants, and thus catalytic activity is reduced or even diminished.

3. Materials and Methods

3.1. Catalyst Preparation

The alumina support was purchased in pellet form from Akzo (Amsterdam, Netherlands), while the ATP support was acquired from a local company in Greece. Both of the supports were calcinated at 800 °C for 4 h. Catalyst preparation was carried out with the wet impregnation technique while using Ni(NO₃)₂·6H₂O aqueous solutions. The targeted Ni concentration was 8 wt.%. The slurries that resulted from preparation were placed in a rotary evaporator, set at 75 °C for 5 h, and then dried at 120 °C for 12 h. The catalysts were then calcined at 800 °C for 4 h; these samples have been denoted throughout this manuscript as “calcined” catalysts. Reduced counterparts were also produced by in situ reduction for 1 h at 800 °C in pure H₂ flow (denoted as “reduced” catalysts).

3.2. Materials Characterization

The ICP measurements were carried out on a Perkin-Elmer Optima 4300DV apparatus (Waltham, MA, USA). The XRD patterns of the catalysts were collected at room temperature while using a Thermo Al (Waltham, MA, USA) powder diffraction system with Cu-K_{α1} radiation operated at 40 kV and 30 mA. The textural characteristics of the catalysts (specific surface area, pore volume) were studied while using a high-resolution 3Flex Micromeritics (Atlanta, GA, USA) porosimeter. The reduction profiles were acquired through H₂ temperature-programmed reduction (H₂-TPR), whereas the acidity/basicity of the surfaces was studied using NH₃-/CO₂-TPD experiments that employed an Autochem 2920, (Micromeritics, Atlanta, GA, USA) unit. Qualitative energy dispersive X-ray spectroscopy (EDS) was conducted with an Oxford XMax^N 50 mm² silicon drift detector that was coupled with the SEM equipment, and an AZtecEnergy analysis software (Oxford Instruments, Abingdon, UK). The aberration corrected scanning transmission electron microscopy (Cs-corrected STEM) images were acquired while using a high angle annular dark field detector in an FEI XFEG TITAN (Waltham, MA, USA) electron microscope operated at 300 kV that was equipped with a CETCOR Cs-probe corrector from CEOS. XPS studies were carried out on a ThermoFisher Scientific Instruments (East Grinstead, UK) K-Alpha⁺ spectrometer while using a monochromated Al K_α X-ray source (hν = 1486.6 eV). Detailed information

regarding the instruments used and methodology followed can be found in previous publications by our group, e.g., [17,27]. The nickel dispersion was estimated while using the Vannice method, following the equation $D_M = 6 \times 10^7 (V_M/A_M) (1/d)$ [58], where D_M is the metal dispersion, V_M is the bulk atomic volume of the metal (cm^3), A_M is the atomic area (cm^2), and d is the metal crystallite size (nm) from XRD.

3.3. Catalytic Tests

The catalytic experiments were carried out in a continuous flow fixed-bed reactor; the exact system and procedure has been described in detail in previous publications, e.g., [17–19,27]. In short, two different experimental protocols were followed, keeping the WHSV at $50,000 \text{ mL g}^{-1} \text{ h}^{-1}$. The first protocol aimed at investigating the effect of temperature on catalytic activity and the second was designed with the purpose of testing catalytic stability. For the former, the temperature range under which the experiments were carried out was between $400\text{--}750 \text{ }^\circ\text{C}$ and the gas feed at the inlet of the reactor was a gas mixture of 73% H_2O , 4% $\text{C}_3\text{H}_8\text{O}_3$, and 23% He (i.e., 20 v.v. % of $\text{C}_3\text{H}_8\text{O}_3$ diluted in H_2O). For the latter (protocol #2), the temperature chosen was $600 \text{ }^\circ\text{C}$, time-on-stream experiments were carried out for a total of 20h, and the gas mixture at the reactor's inlet consisted of 63% H_2O , 7% $\text{C}_3\text{H}_8\text{O}_3$, and 30% He (i.e., 31 v.v. % of $\text{C}_3\text{H}_8\text{O}_3$ diluted in H_2O). The conditions were more severe for the second experimental protocol, as the aim was to induce catalyst deactivation. Before the beginning of the experiments, catalytic activation was undertaken in situ while using a flow (100 mL min^{-1}) of high purity H_2 (5.0) at $800 \text{ }^\circ\text{C}$ for 1 h. Subsequently, the system was purged with He and the temperature was lowered according to the protocol that was to be followed.

The liquid products were analysed via a combination of Gas Chromatography (Agilent 7890A—Santa Clara, CA, USA) and Mass Spectroscopy (Agilent 5975C—Santa Clara, CA, USA). The gaseous products were determined via an Agilent gas chromatographer (7890A). Detailed information regarding the analysis of liquid and gaseous products can be found at ref. [59].

3.4. Reaction Metrics

The calculation of the total glycerol conversion, the conversion of glycerol into gaseous products, and the determination of the H_2 yield and H_2 , CH_4 , CO_2 , and CO selectivity was undertaken while using Equations (13)–(17), as shown below. The selectivity of acetone [$(\text{CH}_3)_2\text{CO}$], acetaldehyde ($\text{C}_2\text{H}_4\text{O}$), acetol ($\text{C}_3\text{H}_6\text{O}_2$), allyl alcohol ($\text{CH}_2=\text{CHCH}_2\text{OH}$), acrolein ($\text{C}_3\text{H}_4\text{O}$), and acetic acid ($\text{C}_2\text{H}_4\text{O}$) was calculated based on Equation (18):

$$\% \text{ glycerol conversion}_{(\text{global conversion})} = ((\text{Glycerol}_{\text{in}} - \text{Glycerol}_{\text{out}})/\text{Glycerol}_{\text{in}}) \times 100 \quad (13)$$

$$\% \text{ glycerol conversion}_{(\text{gaseous conversion})} = (\text{C atoms in the gas products}/\text{total C atoms in the feedstock}) \times 100 \quad (14)$$

$$\text{H}_2 \text{ yield} = \text{H}_2 \text{ mol produced}/\text{mol of glycerol in the feedstock} \quad (15)$$

$$\% \text{ H}_2 \text{ selectivity} = (\text{H}_2 \text{ mol produced}/\text{C atoms produced in the gas phase}) \times (1/\text{RR}) \times 100 \quad (16)$$

where, RR is defined as the ratio of mol of H_2 to CO_2 formed, i.e., the reforming ratio (7/3).

$$\% \text{ selectivity of } i = (\text{C atoms in species } i/\text{C atoms produced in the gas phase}) \times 100 \quad (17)$$

where, species i refers to CO_2 , CO and CH_4 .

$$\% \text{ selectivity of } i' = (\text{C atoms in species } i'/\text{C atoms produced in the liquid phase}) \times 100 \quad (18)$$

where, species i' refers to acetol, acetone, allyl alcohol, acetaldehyde, acrolein, and acetic acid.

4. Conclusions

For the work that is presented herein, attapulgite (natural clay) was used as carrier to produce a nickel-based catalyst (Ni/ATP). Its catalytic performance was comparatively assessed with a standard Ni/Al₂O₃ sample for the glycerol steam reforming reaction. It was shown that the ATP support led to lower mean Ni crystallite size, i.e., it increased the dispersion of the active phase (XPS and TEM), to the easier reduction of NiO (TPR), and also increased the basicity of the catalytic material (TPD). It was also shown that it had a significant effect in the distribution of the gaseous products. Specifically, for the Ni/ATP catalyst, the production of liquid effluents was minimal and, subsequently, the conversion of glycerol into gaseous products was higher. Importantly, the Ni/ATP favored conversion into H₂ and CO₂ to the detriment of CO and CH₄. The stability experiments that were undertaken at a low WGFR showed that the activity of both catalysts was affected with time as a result of carbon deposition and/or metal particle sintering. An examination of the spent catalysts using electron microscopy revealed that the coke deposits consisted of filamentous carbon, a type that is known to encapsulate the active phase with fatal consequences. Being a widely available natural material, ATP is a promising supporting material that is worth further investigating in reforming reactions.

Supplementary Materials: The following are available online at <http://www.mdpi.com/2073-4344/9/8/650/s1>, Figure S1: XPS wide scan spectrum of the reduced Ni/ATP catalyst.

Author Contributions: Conceptualization, N.D.C. and M.A.G.; Data curation, N.D.C., V.S., S.J.H., M.A.B., K.P. and M.A.G.; Formal analysis, N.D.C., V.S., S.J.H., M.A.B., K.P. and M.A.G.; Investigation, N.D.C. and M.A.G.; Methodology, N.D.C. and M.A.G.; Project administration, N.D.C. and M.A.G.; Supervision, N.D.C. and M.A.G.; Validation, N.D.C.; Writing—original draft, N.D.C., M.A.B., K.P. and M.A.G.; Writing—review & editing, M.A.B., K.P. and M.A.G.

Funding: This research received no external funding.

Conflicts of Interest: The authors declare no conflict of interest.

References

1. Silva, J.M.; Ribeiro, L.S.; Orfao, J.J.M.; Soria, M.A.; Madeira, L.M. Low temperature glycerol steam reforming over a Rh-based catalyst combined with oxidative regeneration. *Int. J. Hydrogen Energy* **2019**, *44*, 2461–2473. [[CrossRef](#)]
2. Charisiou, N.D.; Papageridis, K.N.; Siakavelas, G.; Tzounis, L.; Goula, M.A. Effect of active metal supported on SiO₂ for selective hydrogen production from the glycerol steam reforming reaction. *BioResources* **2016**, *11*, 10173–10189. [[CrossRef](#)]
3. Monteiro, M.R.; Kugelmeier, C.L.; Pinheiro, R.S.; Batalha, M.O.; Cesar, A.S. Glycerol from biodiesel production: Technological paths for sustainability. *Renew. Sustain. Energy Rev.* **2018**, *88*, 109–122. [[CrossRef](#)]
4. Bagheri, S.; Julkapli, N.M.; Yehye, W.A. Catalytic conversion of biodiesel derived raw glycerol to value added products. *Renew. Sustain. Energy Rev.* **2015**, *41*, 113–127. [[CrossRef](#)]
5. Schwengber, C.A.; Alves, H.J.; Schaffner, R.A.; da Silva, F.A.; Sequinel, R.; Bach, V.R.; Ferracin, R.J. Overview of glycerol reforming for hydrogen production. *Renew. Sustain. Energy Rev.* **2016**, *58*, 259–266. [[CrossRef](#)]
6. Bagnato, G.; Iulianelli, A.; Sanna, A.; Basile, A. Glycerol Production and Transformation: A Critical Review with Particular Emphasis on Glycerol Reforming Reaction for Producing Hydrogen in Conventional and Membrane Reactors. *Membranes* **2017**, *7*, 17. [[CrossRef](#)] [[PubMed](#)]
7. Charisiou, N.D.; Polychronopoulou, K.; Asif, A.; Goula, M.A. The potential of glycerol and phenol towards H₂ production using steam reforming reaction: A review. *Surf. Coat. Technol.* **2018**, *352*, 92–111. [[CrossRef](#)]
8. Chen, H.; Ding, Y.; Cong, N.T.; Dou, B.; Dupont, V.; Ghadiri, M.; Williams, P.T. A comparative study on hydrogen production from steam-glycerol reforming: Thermodynamics and experimental. *Renew. Energy* **2011**, *36*, 779–788. [[CrossRef](#)]
9. White, R.; Dupont, V.; Cockerill, T. Thermodynamic modelling and energy balance of direct methanation of glycerol for Bio-SNG production. *Energy Convers. Manag.* **2018**, *160*, 354–363. [[CrossRef](#)]
10. Charisiou, N.D.; Papageridis, K.N.; Siakavelas, S.; Tzounis, L.; Kousi, K.; Baker, M.A.; Hinder, S.J.; Sebastian, V.; Polychronopoulou, K.; Goula, M.A. Glycerol steam reforming for hydrogen production over nickel supported on alumina, zirconia and silica catalysts. *Top. Catal.* **2017**, *60*, 1226–1250. [[CrossRef](#)]

11. Goula, M.A.; Charisiou, N.D.; Papageridis, K.N.; Siakavelas, G. Influence of the synthesis method parameters used to prepare nickel-based catalysts on the catalytic performance for the glycerol steam reforming reaction. *Chin. J. Catal.* **2016**, *37*, 1949–1965. [[CrossRef](#)]
12. Menezes da, S.Q.J.P.; Manfro, R.L.; Souza, M.M.V.M. Hydrogen production from glycerol steam reforming over nickel catalysts supported on alumina and niobia: Deactivation process, effect of reaction conditions and kinetic modeling. *Int. J. Hydrogen Energy* **2018**, *43*, 15064–15082. [[CrossRef](#)]
13. Demsash, H.D.; Mohan, R. Steam reforming of glycerol to hydrogen over ceria promoted nickel–alumina catalysts. *Int. J. Hydrogen Energy* **2016**, *41*, 22732–22742. [[CrossRef](#)]
14. Senseni, A.Z.; Meshkani, F.; Rezaei, M. Steam reforming of glycerol on mesoporous nanocrystalline Ni/Al₂O₃ catalysts for H₂ production. *Int. J. Hydrogen Energy* **2016**, *41*, 20137–20146. [[CrossRef](#)]
15. Bobadilla, L.F.; Penkova, A.; Alvarez, A.; Domínguez, M.I.; Romero-Sarria, F.; Centeno, M.A.; Odriozola, J.A. Glycerol steam reforming on bimetallic NiSn/CeO₂–MgO–Al₂O₃ catalysts: Influence of the support, reaction parameters and deactivation/regeneration processes. *Appl. Catal. A Gen.* **2015**, *492*, 38–47. [[CrossRef](#)]
16. Dieuzeide, M.L.; Laborde, M.; Amadeo, N.; Cannilla, C.; Bonura, G.; Frusteri, F. Hydrogen production by glycerol steam reforming: How Mg doping affects the catalytic behaviour of Ni/Al₂O₃ catalysts. *Int. J. Hydrogen Energy* **2016**, *41*, 157–166. [[CrossRef](#)]
17. Charisiou, N.D.; Siakavelas, G.; Tzounis, L.; Dou, B.; Sebastian, V.; Hinder, S.J.; Baker, M.A.; Polychronopoulou, K.; Goula, M.A. Hydrogen production through the glycerol steam reforming reaction: The influence of Y₂O₃ doping on Ni/ZrO₂ catalysts. *Int. J. Hydrogen Energy*. in press. [[CrossRef](#)]
18. Charisiou, N.D.; Siakavelas, G.; Papageridis, K.N.; Sebastian, V.; Hinder, S.J.; Baker, M.A.; Polychronopoulou, K.; Goula, M.A. The influence of SiO₂ doping on the Ni/ZrO₂ supported catalyst for hydrogen production through the glycerol steam reforming reaction. *Catal. Today* **2019**, *319*, 206–219. [[CrossRef](#)]
19. Charisiou, N.D.; Siakavelas, G.; Sebastian, V.; Baker, M.A.; Hinder, S.J.; Polychronopoulou, K.; Goula, M.A. Hydrogen production from the steam reforming of glycerol over Ni catalysts supported on Al₂O₃ and AlCeO₃. *Catalysts* **2019**, *9*, 411. [[CrossRef](#)]
20. Polychronopoulou, K.; Charisiou, N.D.; Siakavelas, G.; AlKhoori, A.A.; Sebastian, V.; Hinder, S.J.; Baker, M.A.; Goula, M.A. Ce–Sm–xCu cost efficient catalysts for H₂ production through the glycerol steam reforming reaction. *Sustain. Energy Fuels* **2019**, *3*, 673–691. [[CrossRef](#)]
21. Polychronopoulou, K.; Charisiou, N.D.; Papageridis, K.N.; Sebastian, V.; Dabbawala, A.A.; AlKhoori, A.A.; Goula, M.A. The effect of Ni addition onto a Cu-based ternary support on the H₂ production over glycerol steam reforming reaction. *Nanomaterials* **2018**, *8*, 931. [[CrossRef](#)] [[PubMed](#)]
22. Rossetti, I.; Gallo, A.; Dal Santo, V.; Bianchi, C.L.; Nichele, V.; Signoretto, M.; Finocchio, E.; Ramis, G.; Di Michele, A. Nickel catalysts supported over TiO₂, SiO₂ and ZrO₂ for the steam reforming of glycerol. *ChemCatChem* **2013**, *5*, 294–306. [[CrossRef](#)]
23. Zamzuri, N.H.; Mat, R.; Amin, N.A.S.; Talebian-Kiakalaieh, A. Hydrogen production from catalytic steam reforming of glycerol over various supported nickel catalysts. *Int. J. Hydrogen Energy* **2017**, *42*, 9087–9098. [[CrossRef](#)]
24. Silva, J.M.; Soria, M.A.; Madeira, L.M. Challenges and strategies for optimization of glycerol steam reforming process. *Renew. Sustain. Energy Rev.* **2015**, *42*, 1187–1213. [[CrossRef](#)]
25. Wang, B.; Xiong, Y.; Han, Y.; Hong, J.; Zhang, Y.; Li, J.; Jing, F.; Chu, W. Preparation of stable and highly active Ni/CeO₂ catalysts by glow discharge plasma technique for glycerol steam reforming. *Appl. Catal. B Environ.* **2019**, *249*, 257–265. [[CrossRef](#)]
26. Veiga, S.; Faccio, R.; Segobia, D.; Apesteguia, C.; Bussi, J. Hydrogen production by crude glycerol steam reforming over Ni–La–Ti mixed oxide catalysts. *Int. J. Hydrogen Energy* **2017**, *42*, 30525–30534. [[CrossRef](#)]
27. Charisiou, N.D.; Papageridis, K.N.; Tzounis, L.; Sebastian, V.; Baker, M.A.; Hinder, S.J.; AlKetbi, M.; Polychronopoulou, K.; Goula, M.A. Ni supported on CaO–MgO–Al₂O₃ as a highly selective and stable catalyst for H₂ production via the glycerol steam reforming reaction. *Int. J. Hydrogen Energy* **2019**, *44*, 256–273. [[CrossRef](#)]
28. Iwasa, N.; Takizawa, M.; Arai, M. Preparation and application of nickel-containing smectite-type clay materials for methane reforming with carbon dioxide. *Appl. Catal. A Gen.* **2006**, *314*, 32–39. [[CrossRef](#)]
29. Wang, Y.; Chen, M.; Liang, T.; Yang, Z.; Yang, J.; Liu, S. Hydrogen Generation from Catalytic Steam Reforming of Acetic Acid by Ni/Attapulgitte Catalysts. *Catalysts* **2016**, *6*, 172. [[CrossRef](#)]

30. Ramirez, J.H.; Costa, C.A.; Madeira, L.M.; Mata, G.; Vicente, M.A.; Rojas-Cervantes, M.L.; López-Peinado, A.J.; Martín-Aranda, R.M. Fenton-like oxidation of Orange II solutions using heterogeneous catalysts based on saponite clay. *Appl. Catal. B Environ.* **2007**, *71*, 44–56. [[CrossRef](#)]
31. Wang, Y.; Chen, M.; Li, X.; Yang, Z.; Liang, T.; Zhou, Z.; Cao, Y. Hydrogen production via steam reforming of ethylene glycol over Attapulgite supported nickel catalysts. *Int. J. Hydrogen Energy* **2018**, *43*, 20438–20450. [[CrossRef](#)]
32. Ayodele, O.B.; Abdullah, A.Z. Exploring kaolinite as dry methane reforming catalyst support: Influences of chemical activation, organic ligand functionalization and calcination temperature. *Appl. Catal. A Gen.* **2019**, *576*, 20–31. [[CrossRef](#)]
33. Jiang, B.; Zhang, C.; Wang, K.; Dou, B.; Song, Y.; Chen, H.; Xu, Y. Highly dispersed Ni/montmorillonite catalyst for glycerol steam reforming: Effect of Ni loading and calcination temperature. *Appl. Therm. Eng.* **2016**, *109*, 99–108. [[CrossRef](#)]
34. Menor, M.; Sayas, S.; Chica, A. Natural sepiolite promoted with Ni as new and efficient catalyst for the sustainable production of hydrogen by steam reforming of the biodiesel by-products glycerol. *Fuel* **2017**, *193*, 351–358. [[CrossRef](#)]
35. Chen, M.; Zhou, Z.; Wang, Y.; Liang, T.; Li, X.; Yang, Z.; Chen, M.; Wang, J. Effects of attapulgite-supported transition metals catalysts on glycerol steam reforming for hydrogen production. *Int. J. Hydrogen Energy* **2018**, *43*, 20451–20464. [[CrossRef](#)]
36. Wang, Y.; Chen, M.; Yang, Z.; Liang, T.; Liu, S.; Zhou, Z.; Li, X. Bimetallic Ni-M (M=Co, Cu and Zn) supported on attapulgite as catalysts for hydrogen production from glycerol steam reforming. *Appl. Catal. A Gen.* **2018**, *550*, 214–227. [[CrossRef](#)]
37. Zhong, X.; Xie, W.; Wang, N.; Duan, Y.; Shang, R.; Huang, L. Dolomite-Derived Ni-Based Catalysts with Fe Modification for Hydrogen Production via Auto-Thermal Reforming of Acetic Acid. *Catalysts* **2016**, *6*, 85. [[CrossRef](#)]
38. Cao, J.L.; Shao, G.S.; Wang, Y.; Liu, Y.; Yuan, Z.Y. CuO catalysts supported on attapulgite clay for low-temperature CO oxidation. *Catal. Commun.* **2008**, *9*, 2555–2559. [[CrossRef](#)]
39. Huang, X.; Xie, A.; Wu, J.; Xu, L.; Luo, S.; Xia, J.; Yao, C.; Li, X. Cerium modified MnTiO_x/attapulgite catalyst for low-temperature selective catalytic reduction of NO_x with NH₃. *J. Mater. Res.* **2018**, *33*, 3559–3569. [[CrossRef](#)]
40. Boudriche, L.; Calvet, R.; Hamdi, B.; Balard, H. Surface properties evolution of attapulgite by IGC analysis as a function of thermal treatment. *Colloids Surf. A* **2012**, *399*, 1–10. [[CrossRef](#)]
41. Sidheswaran, P. Heat-induced structural modifications in palygorskite. *Clay Res.* **2002**, *21*, 27–39.
42. Frini-Srasra, N.; Srasra, E. Effect of heating on palygorskite and acid treated palygorskite properties. *Surf. Eng. Appl. Electrochem.* **2008**, *44*, 43–49. [[CrossRef](#)]
43. Wu, Z.; Zhang, J.; Zhao, X.; Li, X.; Wang, F. Attapulgite-supported magnetic dual acid–base catalyst for the catalytic conversion of lignin to phenolic monomers. *J. Chem. Technol. Biotechnol.* **2018**, *94*, 1269–1281. [[CrossRef](#)]
44. Rosha, P.; Mohapatra, S.K.; Mahla, S.K.; Dhir, A. Biogas reforming for hydrogen enrichment by ceria decorated over nickel catalyst supported on titania and alumina. *Int. J. Hydrogen Energy* **2018**, *43*, 21246–21255. [[CrossRef](#)]
45. Van Olphen, H.; Fripiat, J.J. *Data Handbook for Clay Minerals and Other Non-Metallic Materials*, 1st ed.; Pergamon Press: Oxford, NY, USA, 1979; pp. 1–346.
46. Klopogge, J.T.; Wood, B.J. Baseline studies of the clay minerals society source clays by x-ray photoelectron spectroscopy. *Clay Sci.* **2018**, *22*, 85–94. [[CrossRef](#)]
47. Barr, T.L.; Seal, S.; He, H.; Klinowski, J. X-ray photoelectron spectroscopic studies of kaolinite and montmorillonite. *Vacuum* **1995**, *46*, 1391–1395. [[CrossRef](#)]
48. Lehmann, T.; Wolff, T.; Hamel, C.; Veit, P.; Garke, B.; Seidel-Morgenstern, A. Physico-chemical characterization of Ni/MCM-41 synthesized by a template ion exchange approach. *Micropor. Mesopor. Mater.* **2012**, *151*, 113–125. [[CrossRef](#)]
49. Goula, M.A.; Charisiou, N.D.; Pandis, P.K.; Stathopoulos, V.N. Ni/apatite-type lanthanum silicate supported catalyst for the glycerol steam reforming reaction. *RCS Adv.* **2016**, *6*, 78954–78958. [[CrossRef](#)]
50. Valliyappan, T.; Bakhshi, N.N.; Dalai, A.K. Pyrolysis of glycerol for the production of hydrogen or syn gas. *Bioresour. Technol.* **2008**, *99*, 4476–4483. [[CrossRef](#)]

51. Kitamura, S.; Su-Enaga, T.; Ikenaga, N.O.; Miyake, T.; Suzuki, T. Steam reforming of glycerin using Ni-based catalysts loaded on CaO–ZrO₂ solid solution. *Catal. Lett.* **2011**, *141*, 895–905. [[CrossRef](#)]
52. Polychronopoulou, K.; Giannakopoulos, K.; Efstathiou, A.M. Tailoring MgO-based supported Rh catalysts for purification of gas streams from phenol. *Appl. Catal. B Environ.* **2012**, *111*, 360–375. [[CrossRef](#)]
53. Adhikari, S.; Fernando, S.; Gwaltney, S.R.; To, S.D.F.; Bricka, R.M.; Steele, P.H.; Haryanto, A. A thermodynamic analysis of hydrogen production by steam reforming of glycerol. *Int. J. Hydrogen Energy* **2007**, *32*, 2875–2880. [[CrossRef](#)]
54. Wang, C.; Dou, B.; Jiang, B.; Song, Y.; Du, B.; Zhang, C.; Wang, K.; Chen, H.; Xu, Y. Sorption-enhanced steam reforming of glycerol on Ni-based multifunctional catalysts. *Int. J. Hydrogen Energy* **2015**, *40*, 7037–7044. [[CrossRef](#)]
55. Charisiou, N.D.; Siakavelas, G.; Papageridis, K.N.; Baklavaridis, A.; Tzounis, L.; Polychronopoulou, K.; Goula, M.A. Hydrogen production via the glycerol steam reforming reaction over nickel supported on alumina and lanthana-alumina catalysts. *Int. J. Hydrogen Energy* **2017**, *42*, 13039–13060. [[CrossRef](#)]
56. Thyssen, V.V.; Georgetti, F.; Assaf, E.M. Influence of MgO content as an additive on the performance of Ni/MgO–SiO₂ catalysts for the steam reforming of glycerol. *Int. J. Hydrogen Energy* **2017**, *42*, 16979–16990. [[CrossRef](#)]
57. Sad, M.E.; Duarte, H.A.; Vignatti, C.H.; Padro, C.L.; Apestegua, C.L. Steam reforming of glycerol: Hydrogen production optimization. *Int. J. Hydrogen Energy* **2015**, *40*, 6097–6105. [[CrossRef](#)]
58. Luisetto, I.; Tuti, S.; Battochio, C.; Lo Mastro, S.; Sodo, A. Ni/CeO₂–Al₂O₃ catalysts for the dry reforming of methane: The effect of CeAlO₃ content and nickel crystallite size on catalytic activity and coke resistance. *Appl. Catal. A Gen.* **2015**, *500*, 12–22. [[CrossRef](#)]
59. Papageridis, K.N.; Charisiou, N.D.; Siakavelas, G.; Avraam, D.G.; Tzounis, L.; Kousi, K.; Goula, M.A. Comparative study of Ni, Co, Cu supported on γ -alumina catalysts for hydrogen production via the glycerol steam reforming reaction. *Fuel Process. Technol.* **2016**, *152*, 156–175. [[CrossRef](#)]



© 2019 by the authors. Licensee MDPI, Basel, Switzerland. This article is an open access article distributed under the terms and conditions of the Creative Commons Attribution (CC BY) license (<http://creativecommons.org/licenses/by/4.0/>).